STRUCTURAL BIOLOGY

Molecular recognition and activation of the prostacyclin receptor by anti-pulmonary arterial hypertension drugs

James Jiqi Wang[1,2], Sanshan Jin[3,4], Heng Zhang[1], Youwei Xu[1], Wen Hu[1], Yi Jiang[3,4], Chen Chen[2], Dao Wen Wang[2]*, H. Eric Xu[1,4,5]*, Canrong Wu[1]*

Copyright © 2024 The Authors, some rights reserved; exclusive licensee American Association for the Advancement of Science. No claim to original U.S. Government Works. Distributed under a Creative Commons Attribution NonCommercial License 4.0 (CC BY-NC).

The prostacyclin (PGI_2) receptor (IP) is a G_s-coupled receptor associated with blood pressure regulation, allergy, and inflammatory response. It is a main therapeutic target for pulmonary arterial hypertension (PAH) and several other diseases. Here we report cryo–electron microscopy (cryo-EM) structures of the human IP-G_s complex bound with two anti-PAH drugs, treprostinil and MRE-269 (active form of selexipag), at global resolutions of 2.56 and 2.41 angstrom, respectively. These structures revealed distinct features governing IP ligand binding, receptor activation, and G protein coupling. Moreover, comparison of the activated IP structures uncovered the mechanism and key residues that determine the superior selectivity of MRE-269 over treprostinil. Combined with molecular docking and functional studies, our structures provide insight into agonist selectivity, ligand recognition, receptor activation, and G protein coupling. Our results provide a structural template for further improving IP-targeting drugs to reduce off-target activation of prostanoid receptors and adverse effects.

INTRODUCTION

Prostanoids are a class of oxygenated arachidonic acid metabolites that include prostacyclin (PGI_2), prostaglandin D_2 (PGD_2), prostaglandin $F_{2\alpha}$ ($PGF_{2\alpha}$), prostaglandin E_2 (PGE_2), and thromboxane A_2 (*1*). They provoke diverse biological functions in many tissues and cell types through directly interacting with their corresponding prostanoid receptors: prostacyclin receptor (IP), PGD_2 receptors (DP1 and DP2), PGE_2 receptors (EP1 to EP4), $PGF_{2\alpha}$ receptor (FP), and thromboxane receptor (TP), which constitute a subfamily that belongs to class A G protein–coupled receptor (GPCR) (*2*). IP is a member of prostanoid receptor that is encoded by gene *PTGIR* and is highly expressed in the lung, heart, kidney, and throughout the endothelium and smooth muscle cells of the vascular network (*3*) (https://proteinatlas.org). The endogenous agonist PGI_2 is generated by vascular endothelium. Upon stimulation by PGI_2, IP couples predominantly to the G_s subtype of G proteins, which leads to intracellular cyclic adenosine monophosphate (cAMP) accumulation (*4*). Activated by PGI_2, IP plays a pivotal role in regulating blood pressure, allergic responses, and inflammation, making it a valuable therapeutic target for pulmonary arterial hypertension (PAH) and several other diseases (*5*, *6*).

PAH is a progressive and often fatal disease characterized by chronic cellular proliferation and fibrosis of small pulmonary arteries (*7*, *8*). Unfortunately, it has a dismal prognosis. According to the National Institutes of Health, the median survival of PAH patients without targeted treatment is 2.8 years, and only 34% of patients survive for 5 years (*9*). IP agonists are one of the main therapeutic strategies for PAH targeting pulmonary vasculature signal pathway (*10*–*13*). Sodium salt of PGI_2 (epoprostenol) and its analogs such as iloprost and treprostinil (TRE) were approved by the US Food and Drug Administration (FDA) during 1995–2004 for treatment of PAH (*7*, *14*). However, clinical application of the approved IP agonists was limited by its high rate of side effects, possibly caused by its low selectivity for IP (*15*, *16*). Since then, selective IP agonists have attracted extensive attention and have been developed for the treatment of PAH (*17*). In 2015, an orally selective IP agonist with a nonprostanoid structure was approved by FDA (*17*). Its active form, MRE-269 (MRE; {4-[(5,6-diphenylpyrazinyl) (1-methylethyl) amino] butoxy}-acetic acid), demonstrates relatively higher selectivity for IP than iloprost and TRE and showed significant reduction in composite end point of death and complication related to PAH (*17*). Although having superior selectivity, MRE still partly activates EP2 and EP4, with a dissociation constant of 5 μM (*18*). The lack of selectivity to IP by synthetic agonists causes various side effects such as flushing, cough, headache, and dizziness, which limited the therapeutic use of them (*19*). Therefore, elucidating the molecular mechanisms underlying the functional selectivity of individual prostanoid receptor family members is highly important.

Among the nine prostaglandin receptors, active form structures are now limited to EP2, EP3, EP4, and FP (*20*–*23*). Extensive efforts have been made to clarify how the binding of agonists with various pharmacological profiles regulates IP downstream signaling, and molecular details defining the binding modes of ligands remain largely unknown, partly due to scarce structural information on ligand-bound IP complex. Understanding the mechanism of IP signaling and identifying differences in ligand selectivity of prostaglandin receptors is urgently needed and can provide a structural basis for developing more selective drugs with improved safety and fewer adverse effects.

Here, we present two cryo–electron microscopy (cryo-EM) structures of G protein–coupled IP in complex with TRE and MRE, at global resolutions of 2.56 and 2.41 Å. Combined with functional characterizations of mutated receptors, these structures revealed conserved and divergent mechanisms of ligand binding, receptor activation, and G protein coupling by IP.

[1]State Key Laboratory of Drug Research, Shanghai Institute of Materia Medica, Chinese Academy of Sciences, Shanghai 201203, China. [2]Division of Cardiology, Department of Internal Medicine and Hubei Key Laboratory of Genetics and Molecular Mechanism of Cardiologic Disorders, Tongji Hospital, Tongji Medical College, Huazhong University of Science and Technology, Wuhan 430000, China. [3]Lingang laboratory, Shanghai 200031, China. [4]School of Life Science and Technology, ShanghaiTech University, 201210 Shanghai, China. [5]University of Chinese Academy of Sciences, Beijing 100049, China.
*Corresponding author. Email: wucanrong@simm.ac.cn (C.W.); eric.xu@simm.ac.cn (H.E.X.); dwwang@tjh.tjmu.edu.cn (D.W.W.)

RESULTS

Cryo-EM analysis and overall structure

To facilitate the expression IP-G_s complexes, we used a BRIL tag connected to the N terminus of wild-type (WT) IP. Also, 50 residues (S337 to C386) were truncated from the C terminus of the receptor. We used the NanoBiT tethering strategy (*24*) to stabilize assembly of the IP-G_s complexes by fusing the large subunit (LgBiT) to C termini of IP and complementary peptide (HiBiT) to the C termini of the Gβ subunit. We used apyrase to form a nucleotide-free environment and added Nb35 to further stabilize the agonist-bound IP-G_s complex (*25*). Incubation of TRE/MRE with membranes from cells coexpressing receptors and heterotrimer G_s proteins in the presence of Nb35 enabled efficient assembly of the TRE/MRE-IP-G_s complexes, generating highly homogeneous complex samples for structural studies (Fig. 1, A and B).

The structure of IP-G_s complexes bound to TRE/MRE was determined by single-particle cryo-EM at global resolution of 2.56 and 2.41 Å (Fig. 1A, figs. S1 to S3, and table S1). A high-resolution cryo-EM density map enabled accurate model building for the receptor structure containing residues 4 to 312, except for two invisible residues in the intracellular loop 3 (ICL3) (residues 223 and 231). The density maps are also clear for two agonists, most residues of the G_s heterotrimer, and Nb35 (Fig. 1, A and B).

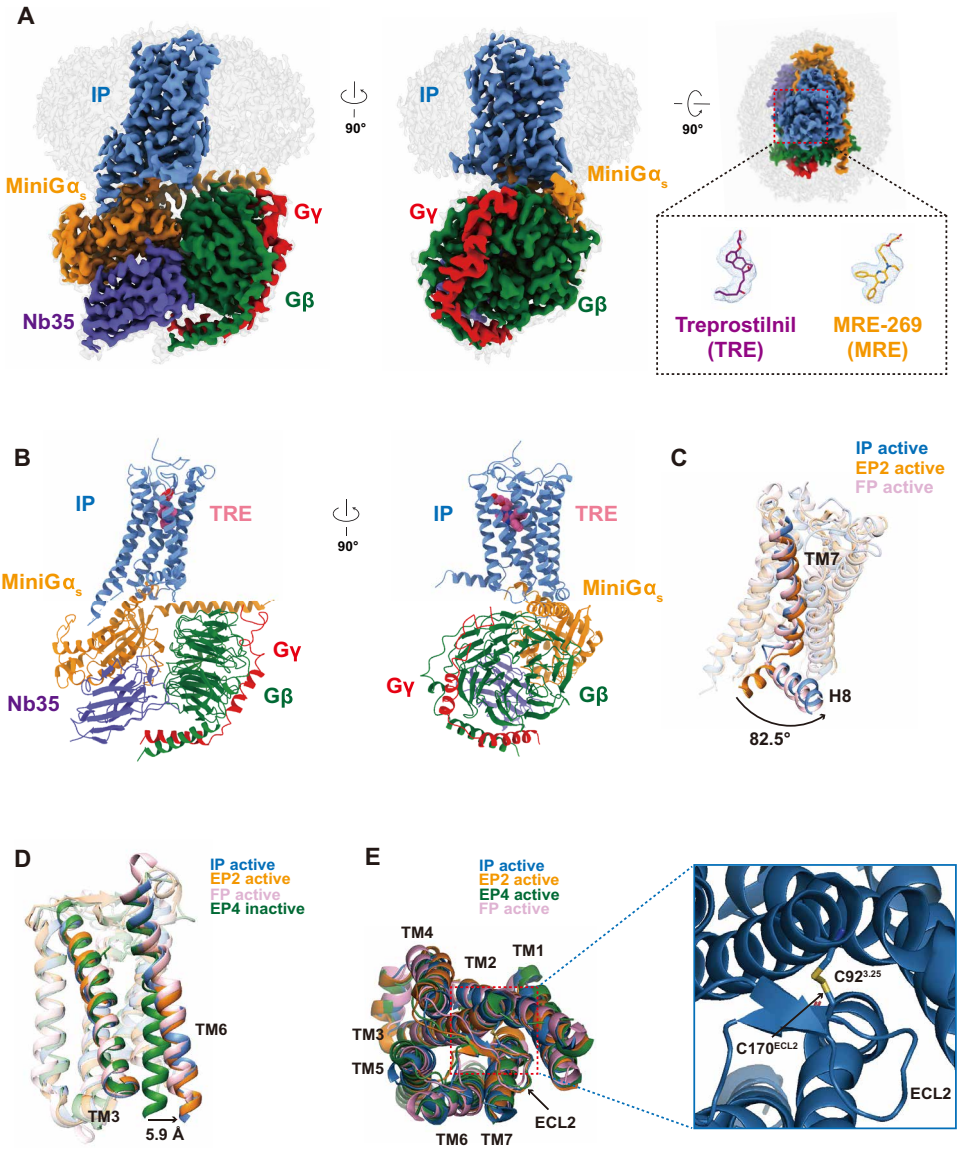

Fig. 1. Cryo-EM structures of IP-G_s complexes. (**A**) Cryo-EM density of IP-G_s complexes bound to TRE or MRE from different view angles. IP, blue; miniGα$_s$, orange; Gβ, green; Gγ, red; Nb35, purple. (**B**) Ribbon representation of TRE-IP-G_s complexes from different view angles. IP, blue; miniGα$_s$, orange; Gβ, green; Gγ, red; Nb35, purple; TRE, pink. (**C**) Comparison of helix 8 (H8) from active IP with active EP2 [Protein Data Bank (PDB) ID: 7CX2] and active FP structure (PDB ID: 8IUK). The direction of the H8 of IP is similar to FP but is different from EP2. IP, blue; EP2, orange; FP, pink. (**D**) Comparison of TM3 and TM6 of active IP (blue) with active EP2 (orange, PDB ID: 7CX2), FP (pink, PDB ID: 8IUK), and inactive EP4 (green, PDB ID: 5YHL). The TM6 of IP showed outward movement compared to inactive EP4. (**E**) Conserved disulfide bond between ECL2 and TM3 in active IP (blue), EP2 (orange, PDB ID: 7CX2), EP4 (green, PDB ID: 7D7M), and FP (pink, PDB ID: 8IUK).

Overall, the active IP adopts the classic seven-transmembrane folding and G protein coupling manner. Helix 8 (H8) of IP was similar to FP but showed an 82.5° rotation compared to EP2 (Fig. 1C). Regarding transmembrane helixes (TMs), activated IP has the canonical outward movement of TM6, which leads to a separation from TM3 (Fig. 1D). The separating distance of TM6 from TM3 and TM7 in IP is similar to activated EP2 and FP (Fig. 1D). At the extracellular interface, the shape of extracellular loop 2 (ECL2) is similar to other prostanoid receptors, forming a β-hairpin loop that is stabilized by the highly conserved disulfide bond between $C92^{3.25}$ and $C170^{ECL2}$ (Fig. 1E). As in other prostanoid receptors, the extracellular region of IP is tightly capped by its β-hairpin ECL2, which mimics those of other prostanoid receptors such as EP2 and FP (Fig. 1E).

Recognition motif of PGI_2 and PGI_2 analog

TRE is a PGI_2 analog approved for PAH therapy with enhanced stability compared to endogenous PGI_2. Thus, it can be administered intravenously, orally, and via inhalation. The well-defined EM density allowed us to accurately assign the α chain, tricyclic ring, and an ω chain of TRE to the corresponding subpockets (Fig. 2, A to C).

The structure of IP bound to the agonist TRE shares important general features with structures of other prostanoid receptors (Fig. 2B and fig. S5A) (*20*) while also exhibiting distinct conformational characteristics. The α chain of TRE fits into a hydrophilic subpocket near the top of the receptor (Fig. 2A) formed by residues from TM1, TM7, and ECL2. The carboxyl group in the α chain of TRE formed a salt bridge with $R279^{7.40}$ and hydrogen bonds with $Y75^{2.65}$ and $S168^{ECL2}$ (Fig. 2, A to C). Alanine mutations of $Y75^{2.65}$, $S168^{ECL2}$, and $R279^{7.40}$ abolished IP activation by TRE (Fig. 2D and fig. S4; no active receptors). Motif $Y75^{2.65}$-$S168^{ECL2}$-$R279^{7.40}$ is conserved among most of the prostanoid receptors (fig. S4). The electrostatic contacts are the major driving force for the interactions between the α chain and the positively charged binding pocket of IP. In region B of TRE, the aromatic ring formed π-π interaction with $W169^{ECL2}$ (Fig. 2, B and C). Hydrophobic residue $V71^{2.61}$ also plays a role in ligand binding by packing with α2 carbon. Mutation of $V71^{2.61}$ and $W169^{ECL2}$ in IP to alanine also significantly reduced the potency of TRE to IP (Fig. 2D and fig. S4). Although IP has the conserved hydrophobic $M/L^{3.32}$-$L/F^{7.36}$ residues, only $L275^{7.36}$ had a significant impact on TRE potency to IP (Fig. 2D and fig. S4). Alanine mutation of $M99^{3.32}$, on the other hand, caused a significantly augmented self-activation (fig. S4). These results suggest that conserved motif $Y75^{2.65}$-$S168^{ECL2}$-$R279^{7.40}$, $W169^{ECL2}$, and $L275^{7.36}$ plays an important role in the TRE-mediated activation of IP.

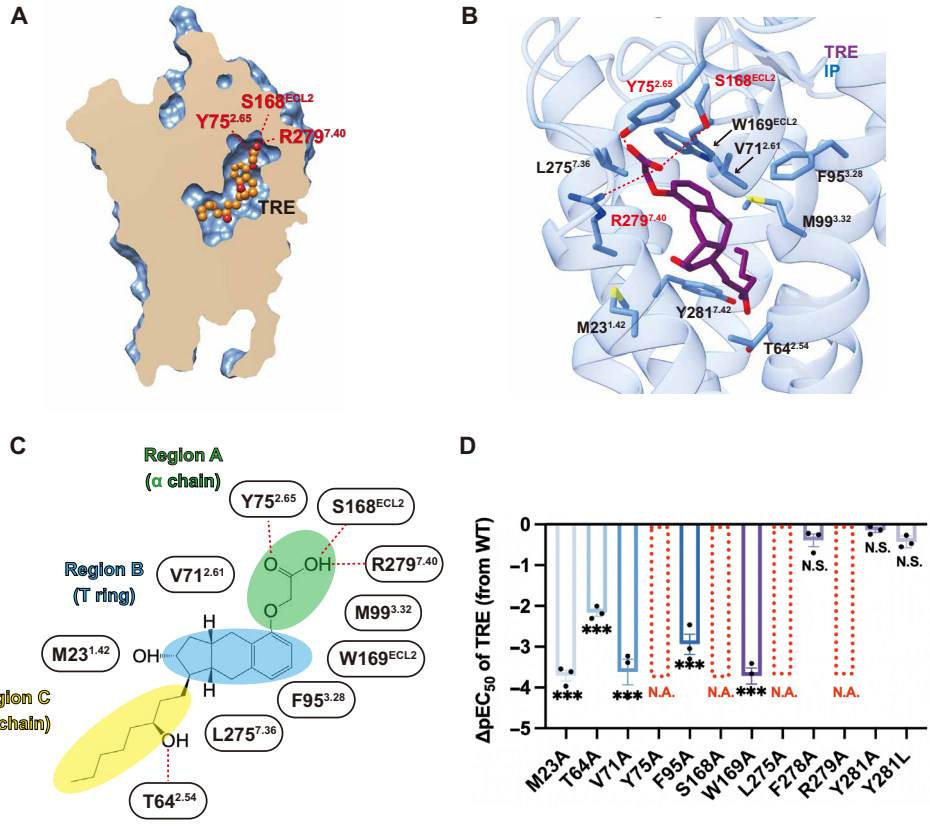

Fig. 2. Binding of PGI_2 analog TRE to IP. (**A**) Vertical cut-through view showing TRE binding pocket in IP. (**B**) Corresponding interactions that contribute to TRE binding in IP. Hydrogen bond is depicted as red dashes. Residues, blue; TRE, purple. (**C**) Region division in IP-TRE binding pockets and corresponding interactions that contribute to the TRE binding with IP. T ring, tricyclic ring. (**D**) cAMP accumulation assay of key mutants of IP that bind to TRE (ΔpEC_{50} = pEC_{50} of agonists to specific mutant IP-pEC_{50} of TRE to WT). Data are presented as mean values ± SEM; $n = 3$ independent samples; significance was determined with one-way analysis of variance (ANOVA); N.A., no active receptors; red dashed-border rectangles, unapplicable ΔpEC_{50} of mutations causing significant reduction of ligand potency that were not able to be calculated; N.S., not significant; ***$P < 0.001$. Exact *P* values and source data are provided as source data file.

To further elucidate the binding mechanisms of IP and its endogenous ligands, we performed molecular docking to predict the pose of PGI_2 bound to IP (fig. S5). The result showed that PGI_2 adopts a similar binding pose as TRE, with predicted binding free energy values (ΔG) of −9.1 kcal/mol (fig. S5, A to C). The carboxyl group in the α chain of PGI_2 also forms hydrogen bonds with $Y75^{2.65}$-$S168^{ECL2}$-$R279^{7.40}$ motif. Compared with TRE, PGI_2 packs weaker with $W169^{ECL2}$, which may explain its lower potency to IP than TRE (*26*, *27*). As reported, other prostanoid ligands like PGE_2 and $PGF_{2\alpha}$ rely heavily on polar contacts with the receptor through oxygen atoms on their cyclopentane rings (fig. S5A). In contrast, PGI_2 contains an additional ether ring that folds the hydroxyl group on region B inward, increasing hydrophobicity of this region. Correspondingly, IP adopts an increased hydrophobic binding pocket formed by unique residues $F72^{2.62}$, $F278^{7.39}$, and $A282^{7.43}$ (fig. S4D) that accommodates PGI_2's hydrophobic region B (fig. S5, B and C), explaining PGI_2's preference for IP. Moreover, unstable PGI_2 is easily hydrolyzed into 6-keto-$PGF_{1\alpha}$, which contains a similar region B to other prostanoids and has weaker potency to IP (*20*, *21*, *28*). To further validate whether the loss of affinity is caused by the structure rearrangement in region B, we performed molecular docking to predict the position of 6-keto-$PGF_{1\alpha}$ bound to IP. The result showed that 6-keto-$PGF_{1\alpha}$ adopts a similar binding pose as PGI_2 with binding free energy values (ΔG) of −7.9 kcal/mol. The weaker affinity may be caused by decreased hydrophobic interactions in hydrolyzed region B (fig. S5D). In summary, these results elucidate IP's unique recognition of PGI_2's hydrophobic region B. Although we observed similar binding position for MRE in the MRE-bound IP structure, substantial differences were found in regions B and C between the MRE and TRE bound IP structures, which will be thoroughly discussed in the next section.

Structural basis of ligand recognition selectivity for IP

Selexipag is a compound distinct from prostanoid analogs and have showed higher selectivity for IP than TRE (*29*). The elevated selectivity could theoretically reduce off-target effects and potentially reduce side effects (*29*). To understand the structural basis of IP ligand selectivity and facilitate future design of selective IP agonists, we determined to cryo-EM structure of IP-G_s complex with the active form of selexipag, MRE-296.

Compared to TRE and other prostanoid receptor ligands (Fig. 3B and fig. S5A), MRE also has a carboxyl end pointing toward outside of the plasma membrane in region A but has a thinner region B and an expanded region C with a pyrazine ring connected to two aromatic rings (Fig. 3, A to C, and fig. S3B). As with TRE, in the region A subpocket, carboxyl end of MRE maintained interaction with $Y75^{2.65}$-$S168^{ECL2}$-$R279^{7.40}$ motif, indicating a similar α chain recognition mode (Fig. 3, A to C, and fig. S4). However, notable disparity of interacting residues exists in region B and C part between MRE and TRE (Fig. 3B). Specifically, TRE formed stronger interaction in region B (Fig. 3E), while MRE formed stronger interactions in region C (Fig. 3F). In region B, TRE exhibited a strong π-π interaction with $W169^{ECL2}$ (Fig. 2C). $W169^{ECL2}$ is highly conserved across all prostanoid receptors except for DP2, elucidating the lack of selectivity displayed by TRE and its capability of activating a wide range of off-target prostanoid receptors. MRE, on the other hand, was more penetrated into IP receptor, avoiding this strong π-π interaction (Fig. 3B). cAMP accumulation assays confirmed that mutation of the $W169^{ECL2}$ had significantly greater impact on the potency of TRE to IP than MRE (Figs. 2D and 3D and fig. S4). This suggests that the conserved $W169^{ECL2}$ plays a bigger role in TRE binding, which partly explains the higher selectivity of MRE. In region C, $Y281^{7.42}$ formed π-π interaction with an aromatic ring in MRE, which was absent in TRE-IP complex. Among the nine prostanoid receptors, IP uniquely has an aromatic tyrosine at position 7.42 (fig. S4D). Other prostanoid receptors contain either alanine or leucine at this residue. This allows MRE to selectively form strong interactions with IP-$Y281^{7.42}$, further contributing to its higher selectivity. cAMP assays confirmed that mutation of $Y281^{7.42}$ to alanine or leucine did not affect potency of TRE for IP but significantly reduced MRE potency (Figs. 2D and 3, D and F, and fig. S4). In summary, the combination of weaker binding to the conserved $W169^{ECL2}$ and stronger binding conferred by unique $Y281^{7.42}$ explains the superior selectivity of MRE.

Residue $T64^{2.54}$ was previously demonstrated to likely participate the potency of EP2 agonist (*21*) and was found in IP, EP2, and EP4. Similarly, both TRE and MRE formed a hydrogen bond with $T64^{2.54}$. Its mutation significantly decreased TRE and MRE potency for IP, partly explaining why MRE can also partly activate EP2 and EP4 (*18*). Moreover, we noticed a marked difference in the direction of $F278^{7.39}$ between TRE and MRE bound IP structures (Fig. 3G). The aromatic ring in $F278^{7.39}$ in MRE-IP showed a 74.5° outward spin compared to TRE-IP. Also, a potential clash lies between MRE and the $F278^{7.39}$ in TRE-IP complex (Fig. 3G). This indicate that $F278^{7.39}$ can sterically hinder the penetration of MRE due to its larger aromatic rings in the region C. Mutation of $F278^{7.39}$ caused a significant increase in MRE potency but did not affect TRE potency (Figs. 2D and 3, D and G), suggesting that removal of this barrier provided more space for its penetration, facilitating this process. Certain modifications could increase ligand potency to IP.

In summary, TRE and MRE share overlapping IP binding mechanisms, with the $Y75^{2.65}$-$S168^{ECL2}$-$R279^{7.40}$ motif and $L275^{7.36}$ mainly contributing to the binding affinity of TRE and MRE. Other residues including $M23^{1.42}$, $T64^{2.54}$, and $V71^{2.61}$also participate in the binding of TRE and MRE (Figs. 2D and 3D). Regarding mechanism of ligand selectivity, MRE achieves superior selectivity by avoiding strong π-π interactions with conserved $W169^{ECL2}$ in region B yet forming strong π-π interaction with $Y281^{7.42}$ in region C (Fig. 3F). Residue $F278^{7.39}$ acted as a sterical hindrance to the pocket entrance of MRE (Fig. 3G). Elucidating ligand selectivity mechanisms of IP provides a framework to design improved selective agonists.

Activation of IP

In comparison with the inactive structure of ONO-AE3-208–bound EP4, the activated IP structure exhibited a large outward shift of TM6, along with an inward shift of TM1, TM5, and a lateral movement of TM7 toward TM6 (Fig. 4A).

As previously reported, a large outward movement of TM6 is the hallmark of GPCR activation. In some cases, GPCR activation results in an outward movement of TM6 and rearrangement of the upper bundle of transmembrane domain via $P^{5.50}$-$I^{3.40}$-$F^{6.44}$ triad motif to stabilize activated structure. However, the canonical $P^{5.50}$-$I^{3.40}$-$F^{6.44}$ triad motif was not seen in IP, which was substituted with $A197^{5.50}$, $M107^{3.40}$, and $M248^{6.44}$ that was sterically too far from each other to form a hydrophobic tight packing (Fig. 4B). Instead, $M107^{3.40}$, $I199^{5.52}$, and $M248^{6.44}$ formed hydrophobic interactions that may play an important role in the connection of the upper bundles of TM3, TM5, and TM6 (Fig. 4C). The rearrangement of TM6 is usually realized through ligand interacting with $W^{6.48}$ toggle switch. However, the $W^{6.48}$ in IP was substituted with $S252^{6.48}$ and did not interact directly with TRE or MRE (fig. S6). This suggests an unconventional

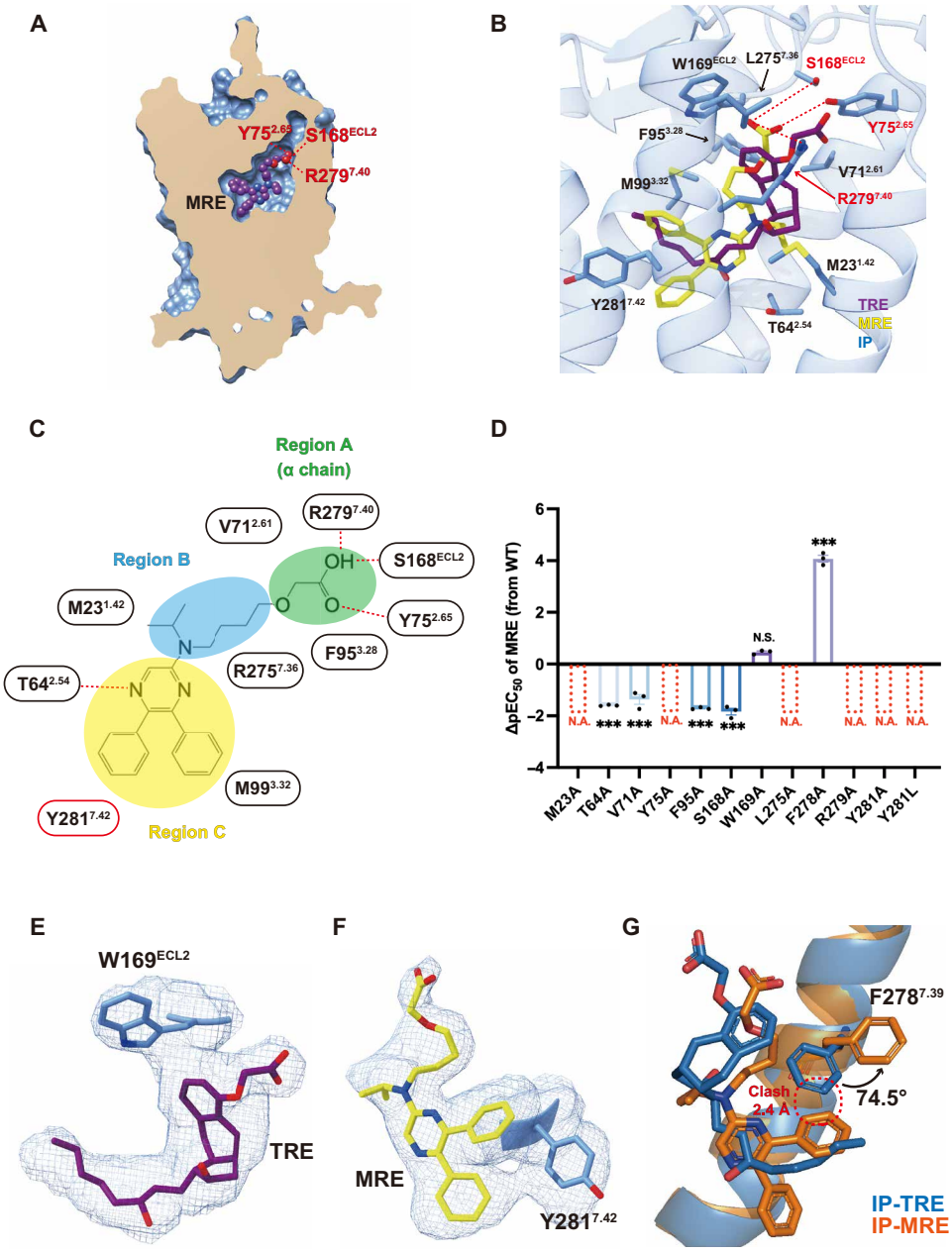

Fig. 3. Binding of MRE to IP. (**A**) Vertical cut-through view showing MRE binding pocket in IP. (**B**) Corresponding interactions that contribute to MRE binding in IP. Hydrogen bond is depicted as red dashes. Residues, blue; MRE, yellow. (**C**) Region division in IP-MRE binding pockets and corresponding interactions that contribute to the MRE binding with IP. (**D**) cAMP accumulation assay of key mutants of IP that bind to MRE (ΔpEC_{50} = pEC_{50} of agonists to specific mutant IP-pEC_{50} of MRE to WT). (**E**) Interaction of W169 in IP with TRE. Residue and ligand are shown in sticks. Correspondent cryo-EM density is represented in mesh. (**F**) Interaction of Y281 in IP with MRE. Residue and ligand are shown in sticks. Correspondent cryo-EM density is represented in mesh. (**G**) Superposition of TRE/MRE-bound IP showing a different direction of F278. Data are presented as mean values ± SEM; $n = 3$ independent samples; significance was determined with one-way ANOVA; N.A., no active receptors; red dashed-border rectangles, unapplicable ΔpEC_{50} of mutations causing significant reduction of ligand potency that were not able to be calculated; N.S., not significant; ***$P < 0.001$. Exact P values and source data are provided as source data file.

mechanism underlying IP activation and outward movement of TM6. As previously mentioned, M23$^{1.42}$ formed interaction with TRE/MRE (Figs. 2B and 3B), causing an inward shift of TM1 (Fig. 4D). Comparison of agonist-bound IP with inactive EP4 reveals several key clashes between the aligned structures. Between TM1 and TM7, one clash occurs between IP-M23$^{1.42}$ and the TM7 backbone of inactive EP4. Another clash is between IP-A26$^{1.45}$ and I323$^{7.47}$ in inactive EP4 (equivalent to I286$^{7.47}$ in IP). These steric clashes appear to drive a lateral movement of TM7 toward TM6. Regarding interaction between TM7 and TM6, IP-F292$^{7.53}$ clashes with the TM6 backbone of inactive EP4, while IP-D288$^{7.49}$ clashes with V281$^{6.44}$ of inactive EP4 (equivalent to M248$^{6.44}$ in IP). These TM6-TM7 clashes likely facilitate

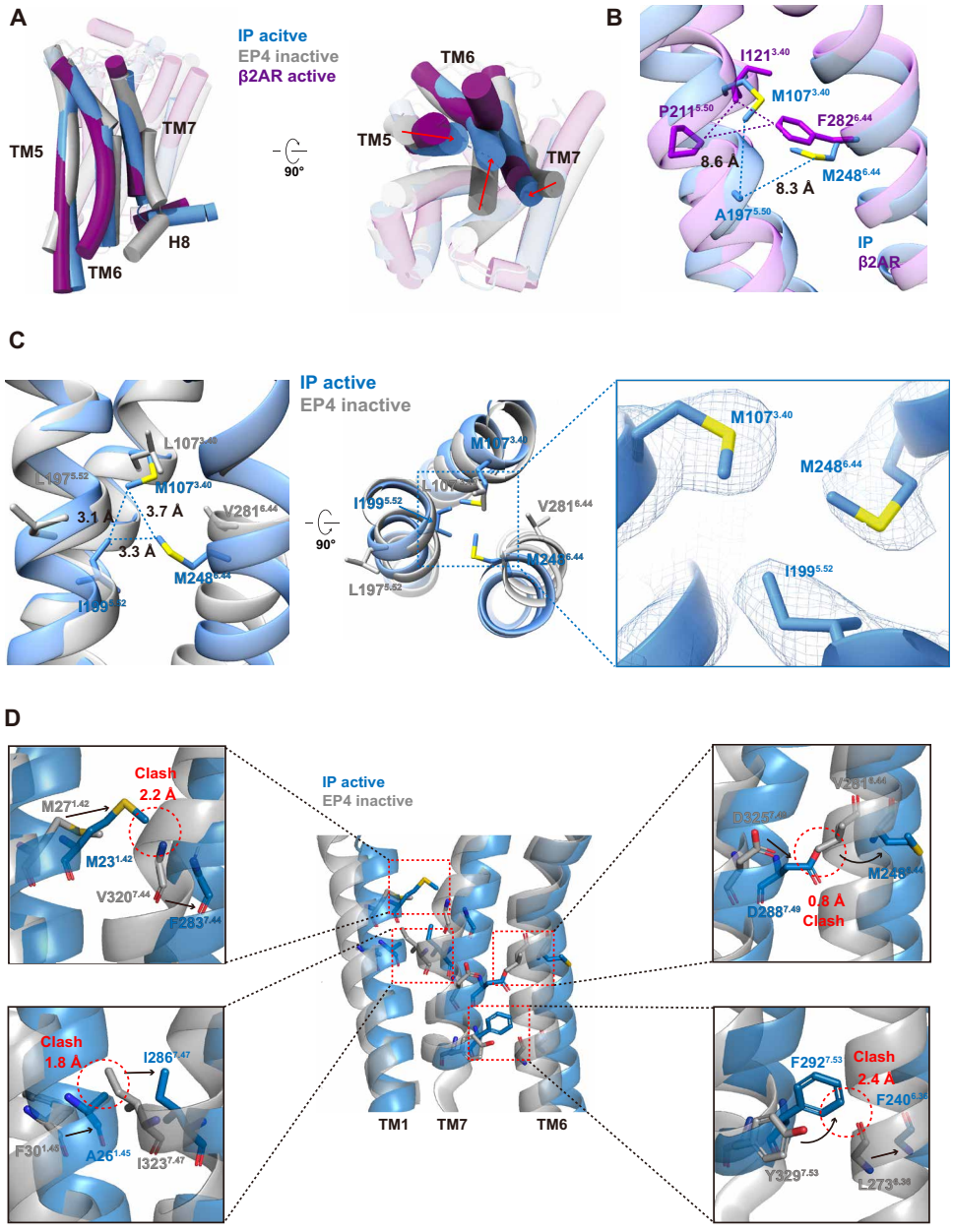

Fig. 4. The active structure of IP. (**A**) Comparison of the G_s-coupled IP with G_s-coupled β2AR (PDB ID: 3SN6) and antagonist-bound inactive EP4 structure (PDB ID: 5YHL) showing position of TM5, TM6, TM7, and H8 helix (helixes are presented as cylinders). (**B**) Superimposition of G_s-coupled IP with G_s-coupled β2AR (PDB ID: 3SN6) aligned at the "PIF motif." (**C**) Superimposition of G_s-coupled IP with antagonist-bound inactive EP4 structure (PDB ID: 5YHL) showing hydrophobic interactions between upper bundles of TM3, TM5, and TM6 in the G_s-coupled IP. (**D**) Superimposition of G_s-coupled IP with antagonist-bound inactive EP4 structure (PDB ID: 5YHL) showing TM movement and interaction of residues during activation. Top left shows clash between M23$^{1.42}$ (IP) and main chain of V320$^{7.44}$ (EP4). Bottom left shows clash between A26$^{1.45}$ (IP) and I323$^{7.47}$ (EP4). Top right shows clash between D288$^{7.49}$ (IP) and main chain of V281$^{6.44}$ (EP4). Bottom right shows clash between F292$^{7.53}$ (IP) and main chain of L273$^{6.36}$ (EP4). IP, blue; β2AR, purple; EP4, gray.

the outward shift of TM6 (Fig. 4D). Mutation of M23$^{1.42}$, M248$^{6.44}$, I286$^{7.47}$, D288$^{7.49}$, and F292$^{7.53}$ significantly impaired IP activation (fig. S6), supporting their proposed roles in enabling the outward movement of TM6 during receptor activation. Together, this formed a propagating activation path subsequently involving TM1, TM7, and TM6 through IP.

At the lower bundle near the cytoplasmic side, IP activation rearranges the ionic lock (D/E$^{3.49}$R$^{3.50}$Y$^{3.51}$, E116$^{3.49}$R117$^{3.50}$C118$^{3.51}$ in IP), which resulted in breaking of the salt bridge formed by E116$^{3.49}$ and R117$^{3.50}$. Notably, R117$^{3.50}$ formed H-bond with N203$^{5.56}$, and the latter interacts with L241$^{6.37}$ (fig. S6), which likely explains the smaller separation distance of TM6 and TM3 in IP compared to β_2AR (Fig. 4A). In addition, IP also had the conserved D288$^{7.49}$P289$^{7.50}$XXY/F292$^{7.53}$ motif and showed obvious structural rearrangement relative to inactive EP4 (fig. S6). Together, these variations stabilized the active conformation of IP.

Assembly of IP-G_s complex

In IP, the outward displacement of TM6 at the cytoplasmic side creates a cavity to accommodate the $G\alpha_s$ subunit. Compare to prototypical β_2AR-G_s and 5-hydroxytryptamine receptor 4-G_s complexes, the shorter separation distance between TM6 and TM3 in IP-G_s complexes (Figs. 4A and 5A) generates a narrower cytoplasmic cavity. Consequently, the $G\alpha_s$ α5 helix tilts 16.5°, inserting more perpendicularly and into the IP cytoplasmic cavity (Fig. 5A), which is similar to other prostanoid receptors (fig. S7A). The buried surface between IP and G_s involved six transmembrane helices (TM1 to TM3 and TM5 to TM7), ICL2, and H8 helix (Fig. 5, A and B). In general, the buried surface of IP with Gα protein (1393.2 $Å^2$) is similar to that of EP4

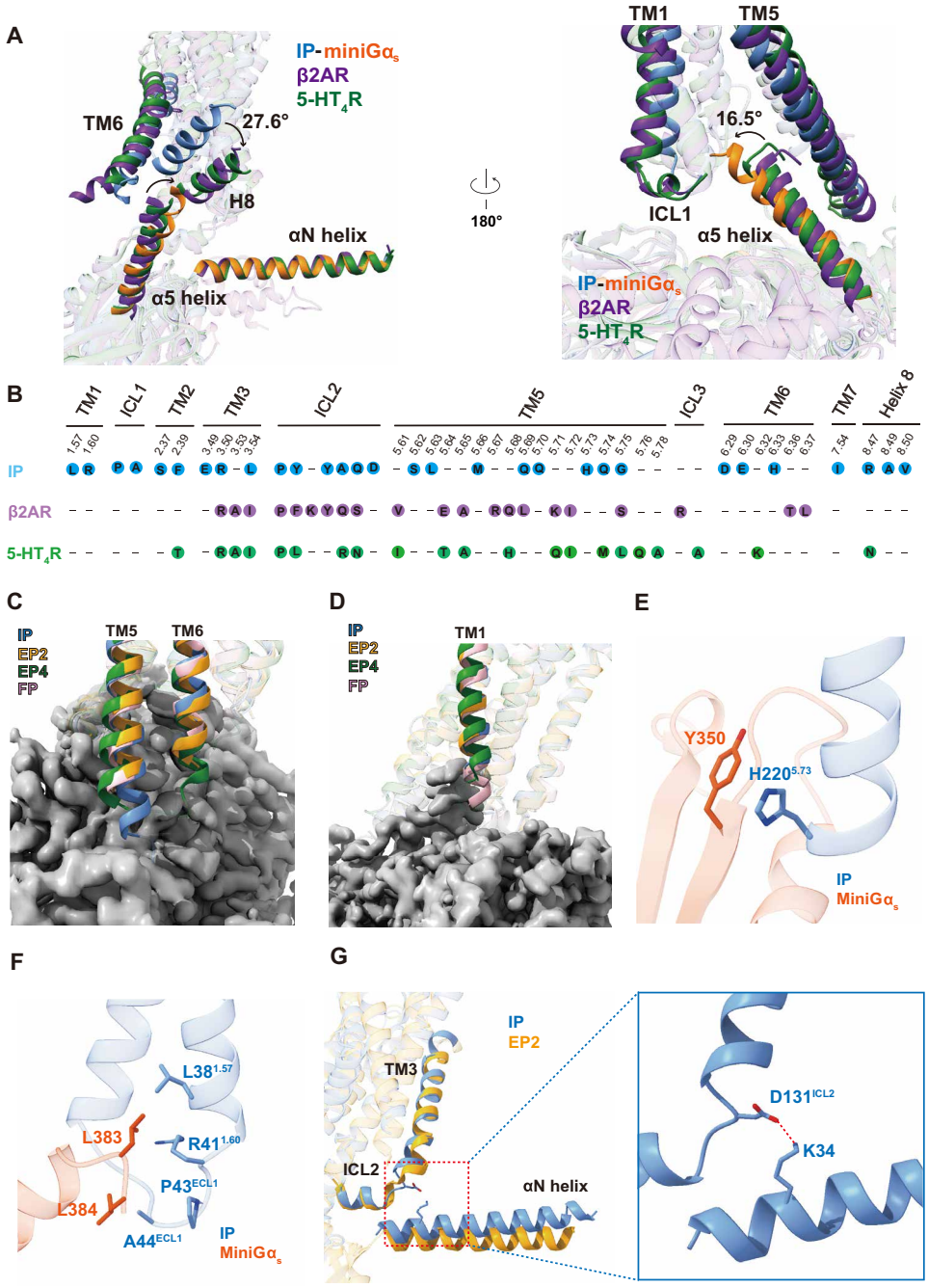

Fig. 5. Structure of IP-G_s coupling. (**A**) Superposition of G_s-coupled IP, β2AR (PDB ID: 3SN6), and 5-HT_4R (PDB ID: 7XT8) complexes according to transmembrane helix bundle. β2AR, purple; 5-HT_4, green; miniGα$_s$ subunit bound to IP, orange; IP, blue. (**B**) G_s coupling interface in IP, β2AR (PDB ID: 3SN6), and 5-HT_4 (PDB ID: 7XT8). (**C**) Comparison of TM5 and TM6 of IP with that of other prostanoid receptors. IP, blue; EP2, light orange; EP4, green; FP, pink. (**D**) Comparison of TM1 of IP with that of other prostanoid receptors. IP, blue; EP2, orange; EP4, green; FP, pink. (**E**) π-π interaction formed by $H220^{5.73}$ in IP and Y350 in miniGα$_s$ subunit. IP, blue; miniGα$_s$, orange. (**F**) Detailed interaction of α5 helix with TM1 and ICL1 from IP. IP, blue; α5 helix, orange. (**G**) Interactions of αN helix of miniG_s with TM3 and ICL2. Red dash indicates salt bridge formed by $D131^{ICL2}$ and K34. IP, blue; EP2, light orange.

(1342.6 Å^2) and FP (1438.5 Å^2) but larger than EP2 (1200.9 Å^2). As previously reported, extended TM5 and shortened TM6 facilitate Gs coupling of GPCRs (*30*). This pattern holds for prostanoid receptors, with IP having the longest TM5 among the G_s-coupled EP2 and EP4 and G_q-coupled FP and a shorter TM6 compared to G_q-coupled FP (Fig. 5, C and D). The relatively elongated TM5 and shortened TM6 of IP compared to the G_q-coupled FP conform with structural features that enable Gs coupling. Specifically, the extended TM5 of IP permits residue H220$^{5.73}$ to form a distinctive π-π interaction with Y350 of $G\alpha_s$ (Fig. 5E) not observed in other prostanoid receptors.

As previously reported, G protein interaction with TM1 and ICL1 is a distinctive feature of prostanoid receptors (*20*–*23*). IP conforms to this pattern, with residues L38$^{1.57}$ and R41$^{1.60}$ interacting with L383 and P43^{ICL1} and P44^{ICL1} interacting with L384, respectively (Fig. 5F). This is likely due to the relatively small outward TM6 movement creating a narrower cavity and rotating the α5 helix toward TM7 and H8 (*20*). Mutation of L38$^{1.57}$ substantially impaired IP activation (fig. S6). In addition, compared to EP2, the αN helix in IP-bound Gα is more closely rotated toward TM3, enabled by a unique salt bridge between D131^{ICL2} in IP and K34 on the αN helix (Fig. 5G). The remainder of the G_s α5 helix is positioned within a cavity formed by TM2 and TM3, ICL2, TM5 and TM6, and H8 (fig. S7, B to D). Notably, R296$^{8.47}$ forms a cation-π interaction with Y381. Mutation of R296$^{8.47}$ to alanine significantly affected IP activation (fig. S6). Together, these distinctive interactions facilitate G protein coupling of IP.

DISCUSSION

Prostanoids are major components of the arachidonic acid metabolism system, whose signaling is known to mediate through nine prostanoid GPCRs. To date, of the nine prostaglandin receptors, active structures bound to G proteins are limited to EP2, EP3, EP4, and FP, with inactive structures known for TP, EP4, and DP2 (*20*–*23*, *31*, *32*). Structural information for the IP receptor is now absent. Uncovering the molecular determinants governing ligand recognition and activation of IP provides fundamental insights critical for developing new therapies for PAH. In this study, we report the cryo-EM structures of IP-G_s complexes bound to its agonists TRE and MRE. Combined with docking analysis and mutagenesis studies, our findings reveal the molecular interactions underlying ligand binding selectivity, activation mechanisms, and G protein coupling that define IP function.

Through structural analysis and functional studies, we identified the structural basis underlying ligand recognition and selectivity of IP. The conserved binding mode of TRE and MRE to IP, mediated through the Y75$^{2.65}$-S168^{ECL2}-R279$^{7.40}$ recognition motif (Figs. 2A and 3A), mirrors that seen for other prostanoid receptors and underscores a shared mechanism of ligand recognition within this receptor family (*20*). Combined with docking analysis, we revealed that the distinct cyclic ether ring in PGI_2 is the key determinant that allowed PGI_2 to binding preferably with IP rather than other prostanoid receptors (fig. S5, C and D). Regarding ligand selectivity, the potent π-π stacking interaction between TRE and the highly conserved W169^{ECL2} not only underlies TRE's increased potency compared with endogenous PGI_2 but also led to TRE's promiscuity across prostanoid receptors. In contrast, MRE achieves superior selectivity over TRE due to its deeper penetrated aromatic rings into the binding pocket (Fig. 3B). This avoids the nonselective π-π stacking with W169^{ECL2} and instead allows MRE to form additional strong π-π stacking with the unique Y281$^{7.42}$ residue at region C (Figs. 2, C and D, and 3, C to F). These distinct binding modes and identification of key determinants for selectivity of IP provide a framework for rational design of improved IP-selective agonists.

IP and three other prostanoid receptors (EP2, EP4, and DP1) contain a serine rather than the canonical tryptophan at toggle switch position 6.48 (fig. S4D), replacing the canonical tryptophan toggle switch residue found in most GPCRs. As with EP2 and EP4 structures, there is no direct interaction between the ligand and TM6, diverging from the conventional mechanism. Activation of EP2 and EP4 is triggered by ligand interactions with TM2 and TM7, respectively (*21*, *28*). Activation of IP, on the other hand, is triggered by ligand interaction with TM1. We elucidated a distinct propagating pathway through TM1, TM7, and TM6 that enables the outward movement of TM6 required for IP activation (Fig. 4D) (*33*). Ligand binding triggers an inward shift of TM1 through interaction with M23$^{1.42}$. This TM1 motion laterally displaces TM7, which in turn pushes TM6 outward to propagate the activating conformational wave through IP (Fig. 4D). This unconventional activation pathway highlights IP's distinct mechanism, diverging from not only the canonical "toggle switch" seen in most GPCRs but also other prostanoid receptors lacking the toggle switch. By elucidating this distinct activating mechanism, our findings reveal IP activates via an atypical route distinct from both classical GPCR activation models and other prostanoid receptors. Like other reported prostanoid receptors, the hydrophobic pack formed by PIF motif in IP is also absent (*20*–*23*, *31*, *32*). We identified an alternative hydrophobic pack constituted by M107$^{3.40}$, I199$^{5.52}$, and M248$^{6.44}$, which further stabilizes the rearranged upper bundle of TM3, TM5, and TM6 in a distinct way. Inspection of the IP-Gs interface revealed unique interactions governing IP-G_s coupling (Fig. 5, A to E). This include π-π stacking of H220$^{5.73}$ with Y350 enabled by the extended TM5 and a salt bridge between D131^{ICL2} and K34 that caused αN helix rotating toward TM3. Moreover, the smaller outward movement of TM6 results in a narrower cavity for α5 helix binding. This caused deeper insertion of α5 helix into cytoplasmic cavity of IP, leading to interactions of the α5 helix with TM1 and ICL1 (Fig. 5A). These interactions are also shared by other prostanoid receptors, suggesting a conserved G protein coupling mode within this receptor family (*20*, *21*, *28*).

It should be noted that although we did attempt to obtain the structure of the endogenous PGI_2-IP-G_s complex, PGI_2 is an extremely unstable compound that rapidly and nonenzymatically hydrolyzes to 6-keto-$PGF_{1\alpha}$, rendering it much less potent toward IP (*34*). This instability prevented further functional studies to investigate IP properties. We used docking studies to help elucidate molecular basis for IP's recognition of its endogenous ligand. The lability of endogenous PGI_2 and the therapeutic importance of IP underscore the need for selective and stable IP agonists. Therefore, elucidating the ligand binding and activation mechanisms of IP, as done in this study, is critical for facilitating the rational design of such agonists.

In summary, our structures clarify the structural basis of ligand selectivity, activation, and G protein coupling for IP. These molecular insights provide a framework to guide design of improved therapies targeting this receptor. Our findings advance understanding of this clinically important IP and may facilitate development of better treatments for PAH and other IP-implicated diseases.

MATERIALS AND METHODS

Construct

We cloned the gene encoding human IP (amino acids 1 to 336) into a pFastBac vector (Thermo Fisher Scientific) using the ClonExpress II One Step Cloning Kit (Vazyme Biotech). To facilitate expression and stabilization, a prolactin signal peptide and BRIL tag were added to the N terminus, and an LgBiT tag was fused to the C terminus. For purification, a 10X histidine tag was fused to the C terminus of IP. Human WT miniGα_s, a human Gβ1 fused with SmBiT at its C terminus, and human Gγ2 were also cloned into pFastBac vectors.

Insect cell expression

Human IP, miniGα_s, Gβ, and Gγ were coexpressed in High Five cells (Hi5, Invitrogen) using the baculovirus method (Expression Systems). Cells were grown in ESF 921 serum-free medium (Expression Systems) at 27°C and 120 rpm to a density of approximately two to three million cells/ml. Cells were then infected with different baculoviruses at a suitable ratio. At 48 hours postinfection, cells were harvested by centrifugation and stored at −80°C.

Protein complex purification

For purification, cells were thawed in 20 mM Hepes (pH 7.4), 150 mM NaCl, 10 mM $MgCl_2$, and $CaCl_2$ with Protease Inhibitor Cocktail (TargetMol). For TRE/MRE-IP-Gα_s-Gβ-Gγ complexes, 10 μM TRE/MRE (MedChemExpress) and 2 mg of Nb35 were added and incubated at room temperature for 1 hour. Membranes were solubilized with 0.5% (w/v) lauryl maltose neopentyl glycol (LMNG; Anatrace) and 0.1% (w/v) cholesteryl hemisuccinate (CHS; Anatrace) at 4°C for 2 hours and then centrifuged at 70,000*g* for 30 min to remove insoluble material. Solubilized complexes were immobilized on nitrilotriacetic acid (Ni-NTA) resin (GenScript), washed with 30 column volumes of wash buffer, and eluted with 300 mM imidazole. Complexes were concentrated using 100-kDa Amicon filters and further purified by size exclusion chromatography on a Superdex 6 Increase 10/300 GL column (GE Healthcare) pre-equilibrated with size buffer containing 20 mM Hepes (pH 7.4),150 mM NaCl, 0.00075% (w/v) LMNG, 0.00025% (w/v) glyco-diosgenin [(GDN) Anatrace], 0.00025% digitonin (w/v), 0.00015% CHS, and 10 μM ligand to separate complexes. Eluted fractions were analyzed by SDS–polyacrylamide gel electrophoresis, and those containing receptor-G_s complexes were pooled, concentrated, and used for cryo-EM.

Cryo-EM grid data collection

Cryo-EM grids were prepared using a Vitrobot Mark IV (FEI) set to 4°C and 100% humidity. Three microliters of sample was applied to glow-discharged R1.2/1.3 gold holey carbon grids and incubated for 10 s before blotting for 3.5 s (double-sided, blot force 2) and rapid freezing in liquid ethane. For the TRE-IP-Gs and MRE-IP-Gs datasets, 8128 and 7994 movie stacks were collected on a 300-kV Titan Krios (Thermo Fisher Scientific) equipped with a Falcon 4 direct electron detector at ×165,000 magnification (0.73 Å pixel size). Data were acquired using EPU software (FEI Eindhoven, The Netherlands) as dose-fractionated movies totaling 50 e^- $Å^{-2}$ over 2.5 s across 36 frames.

Cryo-EM image processing.

We performed motion correction using MotionCor2 to generate drift-corrected micrographs for further processing (*35*, *36*). Contrast transfer function (CTF) parameters were estimated from the micrographs, and particles were picked and extracted for further processing. Two-dimensional (2D) classification, ab initio reconstruction, hetero refinement, nonuniform refinement, local refinement, and local resolution estimation of the particle stacks were carried out in cryoSPARC (*37*).

For TRE-IP-G_s complex dataset, 8128 dose-weighted micrographs were imported into cryoSPARC, and CTF parameters were estimated using patch CTF. Initial template-free particle picking from a subset of micrographs was performed using blob picker, followed by 2D classification to generate templates for template-based autopicking. This resulted in 5,762,832 extracted particles (2.92 Å/pixel). After two rounds of 2D classification, particles in classes showing high-resolution features were selected for ab initio reconstruction and nonuniform refinement, yielding a 3.91-Å map from 119,704 particles. Particles in classes showing poor features were used to generate four low-resolution references for heterogeneous refinement. Using these references, the full set of particles was subjected to four rounds of heterogeneous refinement, resulting in a 3.91-Å map reconstructed from 119,704 particles. Next, 20 classes of 2D templates were generated from 3D maps. Subsequently, 5,196,112 particles were picked by template picker from the full set of micrographs and extracted using a pixel size of 2.92 Å. After two rounds of 2D classification, 1,141,429 particles were selected for four rounds of heterogeneous refinement, resulting in 436,035 particles. These particles were reextracted (0.73 Å/pixel) and subjected to nonuniform and then local refinement, improving the resolution to 2.83 Å. Three rounds of heterogeneous refinement were conducted with updated reference maps, 257,594 particles remained. Following nonuniform refinement, the final map reached a resolution of 2.56 Å.

For MRE-IP-G_s complex dataset, 7994 dose-weighted micrographs were imported into cryoSPARC, and CTF parameters were estimated using patch CTF. Template-based autopicking extracted an initial particle stack of 5,476,773 particles (2.92 Å/pixel). After two rounds of 2D classification, 1,926,128 particles were selected for heterogeneous refinement, which was carried out for four rounds, yielding 340,199 particles. These particles were reextracted at 0.73 Å/pixel and subjected to nonuniform refinement, improving the resolution to 3.04 Å. Further iterative rounds of heterogeneous refinement and nonuniform refinement resulted in a final set of 206,075 particles. Nonuniform refinement and local refinement of this final particle stack led to a 2.41-Å resolution map.

Model building and refinement

We used an AlphaFold2-predicted model of IP as the initial model for building and refinement (*38*). Structures of minG_s, Gβ, Gγ, and the Nb35 derived from Protein Data Bank (PDB) entry 7XW5 (*39*) were rigidly fit into the density map using UCSF Chimera (*40*). The models underwent iterative manual adjustment in COOT (*41*) and automated rebuilding in PHENIX (*42*). The final model was further rebuilt in ISOLDE (*43*) and then refined in PHENIX with torsion angle restraints. Model validation was performed using PHENIX comprehensive validation (cryo-EM) (table S1) (*42*). All structural figures were prepared using Chimera (*40*), Chimera X (*44*), and PyMOL (Schrödinger, LLC.).

cAMP accumulation assay

The full-length WT human IP sequence was subcloned into the pcDNA6.0 vector. The WT and mutant IP constructs (table S2) were transiently transfected into Chinese hamster ovary cells and harvested 24 hours posttransfection. Cell suspensions were dispensed

into white 384-well plates at 5 μl per well before adding 5 μl of ligands. Receptor expression was quantified by flow cytometry using an anti-FLAG Alexa Fluor 488 antibody (Invitrogen, MA1-142-A488). Ligand-induced cAMP accumulation was measured using a LANCE cAMP detection kit (PerkinElmer) per the manufacturer's protocol, with varying ligand concentrations. Fluorescence signals were detected at 620 and 665 nm on an Envision multilabel plate reader (PerkinElmer). Responses were normalized to baseline cAMP levels for each ligand. Half-maximal effective concentration (EC_{50}) values were determined by GraphPad Prism 9.0. Differences in pEC_{50} between mutant and WT receptors (ΔpEC_{50}) were calculated for each agonist. Data represent mean ± SEM of three independent experiments. Differences were considered statistically significant at $^{*}P < 0.05$, $^{**}P < 0.01$, and $^{***}P < 0.001$.

Molecular docking

The TRE-bound IP structure was selected as receptor, the TRE was deleted, and hydrogen atoms were added. Protonation states were assigned using to H++ 3.2v (http://biophysics.cs.vt.edu/H++) at physiological pH 7.4 with AMBER ff 14SB parameters (*45*). Then, protein structure was energy-minimized using the Chiron tool (*46*). The grid line for the docking of IP ligands was of X: 16.833, Y: 12.877, and Z: 14.753 (Angstrom) at the center of X: 130.464, Y: 116.935, and Z: 87.163; the grid box covers almost all the pocket residues. Docking calculations were performed in AutoDock Vina (version 1.1.2) (*47*). The docked protein-ligand structures were visualized in Chimera X software.

Statistics

Data from functional studies were analyzed using GraphPad Prism 9.0 (Graphpad Software Inc.). Results are presented as mean ± SEM of three independent experiments with triplicate measurements. Significance was determined with one-way analysis of variance (ANOVA), and $^{*}P < 0.05$ was considered statistically significant.

Supplementary Materials

This PDF file includes:

Figs. S1 to S7

Tables S1 and S2

REFERENCES AND NOTES

1. B. Wang, L. Wu, J. Chen, L. Dong, C. Chen, Z. Wen, J. Hu, I. Fleming, D. W. Wang, Metabolism pathways of arachidonic acids: Mechanisms and potential therapeutic targets. *Signal Transduct. Target. Ther.* **6**, 94 (2021).
2. D. F. Woodward, R. L. Jones, S. Narumiya, International union of basic and clinical pharmacology. LXXXIII: Classification of prostanoid receptors, updating 15 years of progress. *Pharmacol. Rev.* **63**, 471–538 (2011).
3. D. Claar, T. V. Hartert, R. S. Peebles Jr., The role of prostaglandins in allergic lung inflammation and asthma. *Expert Rev. Respir. Med.* **9**, 55–72 (2015).
4. M. Humbert, E. M. Lau, D. Montani, X. Jais, O. Sitbon, G. Simonneau, Advances in therapeutic interventions for patients with pulmonary arterial hypertension. *Circulation* **130**, 2189–2208 (2014).
5. M. Camacho, C. Rodriguez, A. Guadall, S. Alcolea, M. Orriols, J. R. Escudero, J. Martinez-Gonzalez, L. Vila, Hypoxia upregulates PGI-synthase and increases PGI2 release in human vascular cells exposed to inflammatory stimuli. *J. Lipid Res.* **52**, 720–731 (2011).
6. S. L. Dorris, R. S. Peebles Jr., PGI2 as a regulator of inflammatory diseases. *Mediators Inflamm.* **2012**, 926968 (2012).
7. R. J. Barst, L. J. Rubin, W. A. Long, M. D. McGoon, S. Rich, D. B. Badesch, B. M. Groves, V. F. Tapson, R. C. Bourge, B. H. Brundage, S. K. Koerner, D. Langleben, C. A. Keller, S. Murali, B. F. Uretsky, L. M. Clayton, M. M. Jobsis, S. D. Blackburn, D. Shortino, J. W. Crow, G., A comparison of continuous intravenous epoprostenol (prostacyclin) with conventional therapy for primary pulmonary hypertension. *N. Engl. J. Med.* **334**, 296–301 (1996).
8. M. Humbert, O. Sitbon, A. Chaouat, M. Bertocchi, G. Habib, V. Gressin, A. Yaici, E. Weitzenblum, J. F. Cordier, F. Chabot, C. Dromer, C. Pison, M. Reynaud-Gaubert, A. Haloun, M. Laurent, E. Hachulla, V. Cottin, B. Degano, X. Jais, D. Montani, R. Souza, G. Simonneau, Survival in patients with idiopathic, familial, and anorexigen-associated pulmonary arterial hypertension in the modern management era. *Circulation* **122**, 156–163 (2010).
9. G. E. D'Alonzo, R. J. Barst, S. M. Ayres, E. H. Bergofsky, B. H. Brundage, K. M. Detre, A. P. Fishman, R. M. Goldring, B. M. Groves, J. T. Kernis, P. S. Levy, G. G. Pietra, L. M. Reid, J. T. Reeves, S. Rich, C. E. Vreim, G. W. Williams, M. Wu, Survival in patients with primary pulmonary hypertension. *Ann. Intern. Med.* **115**, 343–349 (1991).
10. H. Olschewski, F. Rose, E. Grunig, H. A. Ghofrani, D. Walmrath, R. Schulz, R. Schermuly, F. Grimminger, W. Seeger, Cellular pathophysiology and therapy of pulmonary hypertension. *J. Lab. Clin. Med.* **138**, 367–377 (2001).
11. S. D. Rybalkin, C. Yan, K. E. Bornfeldt, J. A. Beavo, Cyclic GMP phosphodiesterases and regulation of smooth muscle function. *Circ. Res.* **93**, 280–291 (2003).
12. H. A. Ghofrani, N. Galie, F. Grimminger, E. Grunig, M. Humbert, Z. C. Jing, A. M. Keogh, D. Langleben, M. O. Kilama, A. Fritsch, D. Neuser, L. J. Rubin, PATENT-1 Study Group, Riociguat for the treatment of pulmonary arterial hypertension. *N. Engl. J. Med.* **369**, 330–340 (2013).
13. M. Humbert, H. A. Ghofrani, The molecular targets of approved treatments for pulmonary arterial hypertension. *Thorax* **71**, 73–83 (2016).
14. O. Sitbon, A. Vonk Noordegraaf, Epoprostenol and pulmonary arterial hypertension: 20 years of clinical experience. *Eur. Respir. Rev.* **26**, 160055 (2017).
15. R. P. Camara, F. D. N. Coelho, N. Cruz-Martins, P. Marques-Alves, G. Castro, R. Baptista, F. Ferreira, Incidence of bloodstream infection in patients with pulmonary hypertension under intravenous epoprostenol or iloprost-a multicentre, retrospective study. *Int. J. Mol. Sci.* **24**, 6434 (2023).
16. A. Waxman, R. Restrepo-Jaramillo, T. Thenappan, P. Engel, A. Bajwa, A. Ravichandran, J. Feldman, A. Hajari Case, R. G. Argula, V. Tapson, P. Smith, C. Deng, E. Shen, S. D. Nathan, Long-term inhaled treprostinil for pulmonary hypertension due to interstitial lung disease: INCREASE open-label extension study. *Eur. Respir. J.* **61**, 2202414 (2023).
17. O. Sitbon, R. Channick, K. M. Chin, A. Frey, S. Gaine, N. Galie, H. A. Ghofrani, M. M. Hoeper, I. M. Lang, R. Preiss, L. J. Rubin, L. Di Scala, V. Tapson, I. Adzerikho, J. Liu, O. Moiseeva, X. Zeng, G. Simonneau, V. V. McLaughlin, G. Investigators, Selexipag for the treatment of pulmonary arterial hypertension. *N. Engl. J. Med.* **373**, 2522–2533 (2015).
18. K. Kuwano, A. Hashino, T. Asaki, T. Hamamoto, T. Yamada, K. Okubo, K. Kuwabara, 2-[4-[(5,6-diphenylpyrazin-2-yl)(isopropyl)amino]butoxy]-N-(methylsulfonyl)acetamide (NS-304), an orally available and long-acting prostacyclin receptor agonist prodrug. *J. Pharmacol. Exp. Ther.* **322**, 1181–1188 (2007).
19. M. Kingman, C. Archer-Chicko, M. Bartlett, J. Beckmann, R. Hohsfield, S. Lombardi, Management of prostacyclin side effects in adult patients with pulmonary arterial hypertension. *Pulm. Circ.* **7**, 598–608 (2017).
20. C. Wu, Y. Xu, Q. He, D. Li, J. Duan, C. Li, C. You, H. Chen, W. Fan, Y. Jiang, H. Eric Xu, Ligand-induced activation and G protein coupling of prostaglandin F2α receptor. *Nat. Commun.* **14**, 2668 (2023).
21. C. Qu, C. Mao, P. Xiao, Q. Shen, Y. N. Zhong, F. Yang, D. D. Shen, X. Tao, H. Zhang, X. Yan, R. J. Zhao, J. He, Y. Guan, C. Zhang, G. Hou, P. J. Zhang, G. Hou, Z. Li, X. Yu, R. J. Chai, Y. F. Guan, J. P. Sun, Y. Zhang, Ligand recognition, unconventional activation, and G protein coupling of the prostaglandin E2 receptor EP2 subtype. *Sci. Adv.* **7**, eabf1268 (2021).
22. S. Nojima, Y. Fujita, K. T. Kimura, N. Nomura, R. Suno, K. Morimoto, M. Yamamoto, T. Noda, S. Iwata, H. Shigematsu, T. Kobayashi, Cryo-EM structure of the prostaglandin E receptor EP4 coupled to G protein. *Structure* **29**, 252–260.e6 (2021).
23. K. Morimoto, R. Suno, Y. Hotta, K. Yamashita, K. Hirata, M. Yamamoto, S. Narumiya, S. Iwata, T. Kobayashi, Crystal structure of the endogenous agonist-bound prostanoid receptor EP3. *Nat. Chem. Biol.* **15**, 8–10 (2019).
24. J. Duan, D. D. Shen, X. E. Zhou, P. Bi, Q. F. Liu, Y. X. Tan, Y. W. Zhuang, H. B. Zhang, P. Y. Xu, S. J. Huang, S. S. Ma, X. H. He, K. Melcher, Y. Zhang, H. E. Xu, Y. Jiang, Cryo-EM structure of an activated VIP1 receptor-G protein complex revealed by a NanoBiT tethering strategy. *Nat. Commun.* **11**, 4121 (2020).
25. S. G. Rasmussen, B. T. DeVree, Y. Zou, A. C. Kruse, K. Y. Chung, T. S. Kobilka, F. S. Thian, P. S. Chae, E. Pardon, D. Calinski, J. M. Mathiesen, S. T. Shah, J. A. Lyons, M. Caffrey, S. H. Gellman, J. Steyaert, G. Skiniotis, W. I. Weis, R. K. Sunahara, B. K. Kobilka, Crystal structure of the β2 adrenergic receptor-Gs protein complex. *Nature* **477**, 549–555 (2011).
26. A. M. Siegl, J. B. Smith, M. J. Silver, K. C. Nicolaou, D. Ahern, Selective binding site for [3H] prostacyclin on platelets. *J. Clin. Invest.* **63**, 215–220 (1979).
27. B. J. Whittle, A. M. Silverstein, D. M. Mottola, L. H. Clapp, Binding and activity of the prostacyclin receptor (IP) agonists, treprostinil and iloprost, at human prostanoid receptors: Treprostinil is a potent DP1 and EP2 agonist. *Biochem. Pharmacol.* **84**, 68–75 (2012).
28. S. M. Huang, M. Y. Xiong, L. Liu, J. Mu, M. W. Wang, Y. L. Jia, K. Cai, L. Tie, C. Zhang, S. Cao, X. Wen, J. L. Wang, S. C. Guo, Y. Li, C. X. Qu, Q. T. He, B. Y. Cai, C. Xue, S. Gan, Y. Xie, X. Cong,

Z. Yang, W. Kong, S. Li, Z. Li, P. Xiao, F. Yang, X. Yu, Y. F. Guan, X. Zhang, Z. Liu, B. X. Yang, Y. Du, J. P. Sun, Single hormone or synthetic agonist induces G(s)/G(i) coupling selectivity of EP receptors via distinct binding modes and propagating paths. *Proc. Natl. Acad. Sci. U. S. A.* **120**, e2216329120 (2023).
29. E. M. T. Lau, E. Giannoulatou, D. S. Celermajer, M. Humbert, Epidemiology and treatment of pulmonary arterial hypertension. *Nat. Rev. Cardiol.* **14**, 603–614 (2017).
30. S. Huang, P. Xu, D. D. Shen, I. A. Simon, C. Mao, Y. Tan, H. Zhang, K. Harpsoe, H. Li, Y. Zhang, C. You, X. Yu, Y. Jiang, Y. Zhang, D. E. Gloriam, H. E. Xu, GPCRs steer G(i) and G(s) selectivity via TM5-TM6 switches as revealed by structures of serotonin receptors. *Mol. Cell* **82**, 2681–2695.e6 (2022).
31. H. Fan, S. Chen, X. Yuan, S. Han, H. Zhang, W. Xia, Y. Xu, Q. Zhao, B. Wu, Structural basis for ligand recognition of the human thromboxane A(2) receptor. *Nat. Chem. Biol.* **15**, 27–33 (2019).
32. L. Wang, D. Yao, R. Deepak, H. Liu, Q. Xiao, H. Fan, W. Gong, Z. Wei, C. Zhang, Structures of the human PGD(2) receptor CRTH2 reveal novel mechanisms for ligand recognition. *Mol. Cell* **72**, 48–59.e4 (2018).
33. Q. Zhou, D. Yang, M. Wu, Y. Guo, W. Guo, L. Zhong, X. Cai, A. Dai, W. Jang, E. I. Shakhnovich, Z. J. Liu, R. C. Stevens, N. A. Lambert, M. M. Babu, M. W. Wang, S. Zhao, Common activation mechanism of class A GPCRs. *eLife* **8**, (2019).
34. M. J. Cho, M. A. Allen, Chemical stability of prostacyclin (PGI2) in aqueous solutions. *Prostaglandins* **15**, 943–954 (1978).
35. S. Q. Zheng, E. Palovcak, J. P. Armache, K. A. Verba, Y. Cheng, D. A. Agard, MotionCor2: Anisotropic correction of beam-induced motion for improved cryo-electron microscopy. *Nat. Methods* **14**, 331–332 (2017).
36. A. Rohou, N. Grigorieff, CTFFIND4: Fast and accurate defocus estimation from electron micrographs. *J. Struct. Biol.* **192**, 216–221 (2015).
37. A. Punjani, J. L. Rubinstein, D. J. Fleet, M. A. Brubaker, cryoSPARC: Algorithms for rapid unsupervised cryo-EM structure determination. *Nat. Methods* **14**, 290–296 (2017).
38. K. Tunyasuvunakool, J. Adler, Z. Wu, T. Green, M. Zielinski, A. Zidek, A. Bridgland, A. Cowie, C. Meyer, A. Laydon, S. Velankar, G. J. Kleywegt, A. Bateman, R. Evans, A. Pritzel, M. Figurnov, O. Ronneberger, R. Bates, S. A. A. Kohl, A. Potapenko, A. J. Ballard, B. Romera-Paredes, S. Nikolov, R. Jain, E. Clancy, D. Reiman, S. Petersen, A. W. Senior, K. Kavukcuoglu, E. Birney, P. Kohli, J. Jumper, D. Hassabis, Highly accurate protein structure prediction for the human proteome. *Nature* **596**, 590–596 (2021).
39. J. Duan, P. Xu, X. Luan, Y. Ji, X. He, N. Song, Q. Yuan, Y. Jin, X. Cheng, H. Jiang, J. Zheng, S. Zhang, Y. Jiang, H. E. Xu, Hormone- and antibody-mediated activation of the thyrotropin receptor. *Nature* **609**, 854–859 (2022).
40. E. F. Pettersen, T. D. Goddard, C. C. Huang, G. S. Couch, D. M. Greenblatt, E. C. Meng, T. E. Ferrin, UCSF Chimera—A visualization system for exploratory research and analysis. *J. Comput. Chem.* **25**, 1605–1612 (2004).
41. P. Emsley, K. Cowtan, Coot: Model-building tools for molecular graphics. *Acta Crystallogr. D Biol. Crystallogr.* **60**, 2126–2132 (2004).
42. P. D. Adams, K. Gopal, R. W. Grosse-Kunstleve, L. W. Hung, T. R. Ioerger, A. J. McCoy, N. W. Moriarty, R. K. Pai, R. J. Read, T. D. Romo, J. C. Sacchettini, N. K. Sauter, L. C. Storoni, T. C. Terwilliger, Recent developments in the PHENIX software for automated crystallographic structure determination. *J. Synchrotron Radiat.* **11**, 53–55 (2004).
43. T. I. Croll, ISOLDE: A physically realistic environment for model building into low-resolution electron-density maps. *Acta. Crystallogr. D Struct. Biol.* **74**, 519–530 (2018).
44. E. F. Pettersen, T. D. Goddard, C. C. Huang, E. C. Meng, G. S. Couch, T. I. Croll, J. H. Morris, T. E. Ferrin, UCSF ChimeraX: Structure visualization for researchers, educators, and developers. *Protein Sci.* **30**, 70–82 (2021).
45. J. C. Gordon, J. B. Myers, T. Folta, V. Shoja, L. S. Heath, A. Onufriev, H++: A server for estimating pKas and adding missing hydrogens to macromolecules. *Nucleic Acids Res.* **33**, W368–W371 (2005).
46. S. Ramachandran, P. Kota, F. Ding, N. V. Dokholyan, Automated minimization of steric clashes in protein structures. *Proteins* **79**, 261–270 (2011).
47. O. Trott, A. J. Olson, AutoDock Vina: Improving the speed and accuracy of docking with a new scoring function, efficient optimization, and multithreading. *J. Comput. Chem.* **31**, 455–461 (2010).

Acknowledgments: The cryo-EM data were collected at the Shanghai Advanced Center for Electron Microscopy, Shanghai Institute of Materia Medica, Chinese Academy of Sciences. We thank Q. Yuan, K. Wu, S. Zhang, and S. Li for performing cryo-EM data collection. **Funding:** This work was partially supported by CAS Strategic Priority Research Program (XDB37030103 to H.E.X.); The National Natural Science Foundation of China (32301016 to C.W., 32130022 to H.E.X., 82121005 to H.E.X., 32171187 to Y.J., 82121005 to Y.J., 82330010 to D.W.W., 81902085 to Y.X.); Shanghai Municipal Science and Technology Major Project (2019SHZDZX02 to H.E.X.); the National Key R&D Program of China (2022YFC2703105 to H.E.X.); China Postdoctoral Science Foundation Funded Project (2021M703342 to C.W.); Shanghai Post-doctoral Excellence Program (2021429 to C.W.); Key tasks of Lingang Laboratory (LG202101-01-03 to Y.X., LG202101-01-640 to Y.J.); Grant No. LG-GG-202204-01 (Y.J. and H.E.X.); the author C.W. gratefully acknowledges the support from the Sanofi Scholarship Program. **Author contributions:** J.J.W., Y.X., Y.J., C.C., D.W.W, H.E.X., and C.W. contributed to the formulation and conceptualization of this study. J.J.W., Y.X., Y.J., D.W.W., H.E.X., and C.W. administrated the project. J.J.W and C.W. designed the expression constructs, purified the proteins, and performed cryo-EM grid preparation supervised by Y.J. and H.E.X. C.W. performed data processing and model building. J.J.W. constructed all the mutated plasmids. J.J.W., S.J., Y.X., H.Z., D.W.W., H.E.X., and C.W. contributed to the development of methodology in protein purification and functional studies. J.J.W. and S.J. performed functional studies. J.J.W., C.W., and H.E.X. analyzed the structures. Y.X. and H.Z. provided consult for data processing. W.H. performed cryo-EM data collection and motion correction. J.J.W., S.J., Y.X., H.Z., W.H., D.W.W., and C.W. contributed to the formal analysis of this study. C.W. and H.E.X. conceived project and initiated collaborations with D.W.W. Data validation was conducted by J.J.W., S.J., Y.X., and D.W.W. All authors discussed and commented on the manuscript. J.J.W., H.E.X., and C.W. prepared the figures, and J.J.W. prepared the initial manuscript. C.C. and H.E.X. also contributed to the writing of the initial draft. J.J.W., C.W., H.E.X., D.W.W., and Y.J. revised the manuscript. Y.J., D.W.W., H.E.X., and C.W. contributed to funding acquisition to support this study. **Competing interests:** The authors declare that they have no competing interests. **Data and materials availability:** All data needed to evaluate the conclusions in the paper are present in the paper and/or the Supplementary Materials. The atomic coordinates and cryo-EM density maps have been deposited in the PDB and Electron Microscopy Data Bank (EMDB) under accession numbers 8X7A and EMD-38096 for the TRE-IP complex and 8X79 and EMD-38095 for the MRE-IP complex.

Submitted 26 August 2023
Accepted 10 January 2024
Published 9 February 2024
10.1126/sciadv.adk5184